Computers, Materials & Continua CMC, vol.64, no.2, pp.701-727, 2020

Efficient 2D Analysis of Interfacial Thermoelastic Stresses in Multiply Bonded Anisotropic Composites with Thin Adhesives

Yui-Chuin Shiah[1, *], Sheng-Chi Huang[1] and M. R. Hematiyan[2]

Abstract: In engineering practice, analysis of interfacial thermal stresses in composites is a crucial task for assuring structural integrity when sever environmental temperature changes under operations. In this article, the directly transformed boundary integrals presented previously for treating generally anisotropic thermoelasticity in two-dimension are fully regularized by a semi-analytical approach for modeling thin multi-layers of anisotropic/isotropic composites, subjected to general thermal loads with boundary conditions prescribed. In this process, an additional difficulty, not reported in the literature, arises due to rapid fluctuation of an integrand in the directly transformed boundary integral equation. In conventional analysis, thin adhesives are usually neglected due to modeling difficulties. A major concern arises regarding the modeling error caused by such negligence of the thin adhesives. For investigating the effect of the thin adhesives considered, the regularized integral equation is applied for analyzing interfacial stresses in multiply bonded composites when thin adhesives are considered. Since all integrals are completely regularized, very accurate integration values can be still obtained no matter how the source point is close to the integration element. Comparisons are made for some examples when the thin adhesives are considered or neglected. Truly, this regularization task has laid sound fundamentals for the boundary element method to efficiently analyze the interfacial thermal stresses in 2D thin multiply bonded anisotropic composites.

Keywords: Multiply bonded composites, 2D anisotropic elasticity, boundary element method, regularization of boundary integrals, thermal loading.

1 Introduction

Nowadays, anisotropic composites have been widely applied for various purposes in engineering practice. For applications, they are usually made of different materials, either anisotropic or isotropic, for pursuing ultimate performance. Multiply bonded composites are often made of different anisotropic materials, bonded with very thin layers of isotropic adhesives. It is quite often to encounter significant thermal loads present due to a drastic temperature change in the operational environment. For the mismatch of CTE

[1] Department of Aeronautics and Astronautics, National Cheng Kung University, Tainan, 701, Taiwan.

[2] Department of Mechanical Engineering, Shiraz University, Shiraz, 71936, Iran.

[*] Corresponding Author: Yui-Chuin Shiah. Email: ycshiah@mail.naku.edu.tw.

Received: 04 March 2020; Accepted: 13 April 2020.

(coefficients of thermal expansion) between adjacent materials, significant thermal stresses shall occur at bonding interfaces when the composites are subjected to thermal loads. Consequently, analysis of the interfacial thermal stresses appears to be crucial to prevent potential debonding from thermal loads. In industries, dissimilarly adjoined composites such as laminated composites have been extensively used, see the example Yu et al. [Yu, Tokovyy and Ma (2017)]. So far, many pertinent works have been presented for evaluating interlaminar stresses of layered composites. Despite a few analytical works existing for a few particular cases, see the example Dhaliwal et al. [Dhaliwal and Sherief (1980); Bian, Liu and Pan (2017)], resort to numerical analysis is necessary for general problems, complicated in both geometric domains and boundary conditions. For too many to be mentioned as a thorough review, only a few among them are mentioned here. Lajczok [Lajczok (1986)] calculated interlaminar shear stresses by applying the finite difference scheme to the strains from analysis in the NASTRAN to calculate their derivatives for evaluating interlaminar shear stresses. By an analysis using the finite element method, Tolson et al. [Tolson and Zabaras (1991)] predicted the progressive failure of structure with assessment of interlaminar stresses in laminated composites. By using a higher-order shear deformation theory, Lo et al. [Lo, Christensen and Wu (1978)] calculated the transverse stress components. For a selective review of pertinent works on the interlaminar stresses of composites, the reader may refer to Kant et al. [Kant and Swaminathan (2000)].

In general, conventional modeling thin media by domain techniques will need overwhelming amounts of very refined elements, often leading to retarded computation. Alternatively, the boundary element method, usually abbreviated as the BEM, is very efficient for engineering analysis for its typical nature of boundary discretization; however, its application to the interlaminar stresses has remained comparably scarce indeed. Despite the generality of 3D modeling, the typical analysis of plane-strain or plane-stress has still remained to be a common category for simplifying 3D problems. As a matter of fact, the BEM study of 3D thin anisotropic structures has not yet been explored so far, although their general elastostatic analysis have been intensively investigated by the leading author, see the examples Shiah et al. [Shiah, Tuan and Hematiyan (2018)], [Shiah and Hematiyan (2018)] and [Shiah (2016)]. Also, the BEM thermoelastic analysis for 2D thin anisotropic media remains unexplored so far. The present work aims to fully regularize the 2D boundary integral equation (BIE) for analysis of interlaminar thermal stresses in thin anisotropic composites. As a key issue in the BEM, the problem of the so called "near-singularity" will arise in the BIE when the medium is very thin as compared with its characteristic dimension. This is because of the special condition that the source position on a side is very near an element for integration on its opposite side of a thin medium. Another source of modeling difficulty for the 2D thermoelastic analysis by the BEM originates from the additional volume integral due to thermal effects. Any attempt to directly evaluate it will inevitable require domain integration, shattering the most advantageous notion of boundary discretization. For fully recovering the BEM's notion of boundary discretization, Shiah et al. [Shiah and Wang (2016)] presented a direct volume-to-surface integral transformation. Similarly, the extra volume integral arising from inertial effects has been transformed to the boundary [Shiah and Ye (2016)]. There have been other new methods presented recently to directly compute domain integrals. To name a few as examples, Wen et al. [Wen, Alliabadi

and Rooke (1998)] presented a novel approach to transform domain integral to the boundary. Like the dual reciprocity method, this approach applies the radial base functions to approximate the additional volume integral term. Also, it is worth mentioning that the meshless methods, emerging recently, are very efficient in treating the singularity problems [Lin, Chen and Wang (2014); Lin, Chen and Chen (2014)], and Lin et al. [Lin, Zhang, Sun et al. (2018)]. The present work only targets regularization of the exactly transformed BIE and thus, no detailed review is given to all other pertinent methodologies, although very effective in modeling.

As has been presented in Shiah et al. [Shiah and Wang (2016)], the additional volume integral arising from thermal effects can be exactly transformed onto the boundary; however, there is still one more issue remaining to be resolved for thin anisotropic medium, that is, regularization of the transformed BIE. In the course of regularizing it, the authors have spotted an additional difficulty. For those regarding the radial distance, the scheme of integration by parts can be applied; another integral reveals rapid fluctuation but not near-singularity in its integrand when the source is very near the field point. For regularizing the transformed BIE, those integrals associated with the radial distance are treated by the approach presented previously, while the other one expressed in terms of the polar angle is evaluated by a semi-analytical approach. As demonstrations of our successful implementations in the BEM, a few typical examples are presented in the end.

2 Transformed BIE for 2D anisotropic thermoelasticity

In a statically coupled manner to treat thermoelasticity, the associated thermal field with prescribed boundary conditions needs to be firstly solved to provide thermal data on boundary nodes, including the temperature rise and its gradients in all directions. For anisotropic media, the 2D thermal field without the presence of heat source is governed by

$$\mathrm{K}_{ij}\Phi_{,ij} = 0 \qquad (i,j=1,2), \tag{1}$$

where K_{ij} are conductivity coefficients and Φ is the temperature change. For simplifying the analysis, Eq. (1) can be linearly transformed to the typical Laplace equation as presented in Shiah et al. [Shiah and Wang (2016)]. By the usual collocation process in the BEM, the BIE for "isotropic" potential problems can thus be solved to obtain the thermal data on all boundary nodes, required for the subsequent thermoelastic analysis. Since the present work is not targeted on the analysis of heat conduction, no further discussion about it will be addressed here. In the subsequent elastic analysis, all thermal data on boundary nodes will be taken as prescribed known values.

Having been well established in the literature, the BIE for elastostatic analysis for relating displacements, u_i, and tractions, t_i, between the source P and the field Q on the boundary S (or the field q inside the domain Ω), is expressed as

$$\begin{aligned} &C_{ij}(P)u_i(P) \\ &= \int_S U_{ij}^*(P,Q)\,t_i(Q)\,dS - \int_S T_{ij}^*(P,Q)\,u_i(Q)\,dS + \int_S \gamma_{ik}n_k\Phi(Q)U_{ij}^*(P,Q)\,dS, \\ &-\int_\Omega \gamma_{ik}\Phi_{,k}(Q)U_{ij}^*(P,q)\,d\Omega \end{aligned} \tag{2}$$

where C_{ij} are free coefficients, γ_{ik} are thermal modulii, n_k are unit outward normal components on Q. In Eq. (2), U_{ij}^* and T_{ij}^* are fundamental solutions of displacements and tractions, respectively; their formulations [Lekhnitskii (1981)] are given by

$$U_{ij}^*(P,Q/q) = 2\,\mathrm{Re}\left\{\sum_{k=1}^{2}\alpha_{ik}B_{jk}\ln Z_k\right\}, \tag{3a}$$

$$T_{1j}^*(P,Q) = 2n_1\,\mathrm{Re}\left\{\sum_{k=1}^{2}\frac{\mu_k^2 B_{jk}}{Z_k}\right\} - 2n_2\,\mathrm{Re}\left\{\sum_{k=1}^{2}\frac{\mu_k B_{jk}}{Z_k}\right\}, \tag{3b}$$

$$T_{2j}^*(P,Q) = -2n_1\,\mathrm{Re}\left\{\sum_{k=1}^{2}\frac{\mu_k B_{jk}}{Z_k}\right\} + 2n_2\,\mathrm{Re}\left\{\sum_{k=1}^{2}\frac{B_{jk}}{Z_k}\right\}, \tag{3c}$$

where $\mathrm{Re}\{.\}$ represents taking the real part of a complex variable inside the curly bracket, μ_k are complex roots of the characteristic equation, and α_{ik} and B_{jk} are complex quantities associated with material constants. In Eqs. (3a)-(3c), Z_k are generalized complex variables defined by the Cartesian coordinates of the source point (x_1, x_2) and those of the field point ($\overline{x}_1, \overline{x}_2$), that is

$$Z_j = (x_1 - \overline{x}_1) + \mu_j(x_2 - \overline{x}_2), \tag{4}$$

In Eq. (2), the last integral is a volume integral that needs to be evaluated for each source point. Any effort to evaluate this additional volume integral directly will inevitably require discretization over the entire domain, which is a contradictory notion to the BEM's nature. Among all methodologies for avoiding the domain discretization, the exact transformation approach Shiah et al. [Shiah and Wang (2016)] is perhaps the most analytically elegant. In that process of performing the volume-to-surface integral transformation, the treatment in Shiah et al. [Shiah and Wang (2016)] undertook a technique of domain mapping to transform the additional volume integral onto distorted boundary via a linear coordinate transformation. The transformed BIE for treating generally anisotropic thermoelasticity takes the following form:

$$\begin{aligned} C_{ij}u_i &= \int_S U_{ij}^* t_i\, dS - \int_S T_{ij}^* u_i\, dS + \int_S \gamma_{ik} n_k \Phi\, U_{ij}^*\, dS \\ &+ \int_s \left[\left(\gamma_{\underline{ik}}\, Q_{\underline{ijk},\underline{t}}^* \Phi - \gamma_{\underline{ik}}\, Q_{\underline{ijk}}^* \Phi_{,\underline{t}}\right) n_{\underline{t}} - \gamma_{\underline{ik}} U_{\underline{ij}}^* \Phi\, n_{\underline{k}}\right] d\hat{S}' \end{aligned} \tag{5}$$

where (P, Q) are omitted for simplification, the underline in the subscripts refers to the new coordinates for the domain mapping, and $Q_{\underline{ijk}}^*$ is an auxiliary function to facilitate the volume-to-surface integral transformation. More details about the above transformed BIE can be referred to Shiah et al. [Shiah and Wang (2016)]. It is worth mentioning that there is no extra line integral involved in Eq. (5) for resolving the discontinuity issue of the multi-valued function in the fundamental solutions. As a main shortcoming in Eq. (5), the domain mapping undertaken for the volume-to-surface integral transformation requires extra process of coordinate transformation, making the transformed BIE in Eq.

(5) less appealing, although the involved computation efforts for that are very trivial indeed. In light of the complexity added by taking the intermediate coordinate transformation, Shiah et al. [Shiah, Hsu and Hwu (2018)] presented a new direct transformation, not depending on any domain mapping; it is expressed as follows:

$$C_{ij}u_i = \int_\Gamma U_{ij}^* t_i \, dS - \int_\Gamma T_{ij}^* u_i dS + \mathrm{K}_{ik} \int_\Gamma (\Phi G_{j,k}^* n_i - G_j^* \Phi_{,i} n_k) \, dS \,, \tag{6}$$

where G_j^* is a new function designed for making the analytical transformation, expressed in the following series form:

$$G_i^*(r,\theta) = 2r \ln r \left(\overline{\Re}_i^{(1)} \cos\theta - \overline{\Im}_i^{(1)} \sin\theta \right) + 2r \sum_{n=2}^{m} \left(\overline{\Re}_i^{(n)} \cos n\theta - \overline{\Im}_i^{(n)} \sin n\theta \right), \tag{7}$$

In Eq. (7), (r, θ) represent the polar coordinates with origin settled at the source point, and $\overline{\Re}_i^{(n)} / \overline{\Im}_i^{(n)}$ denote taking the real/imaginary part of a series of constants, obtained by solving a system of simultaneous equation as elaborated in Shiah et al. [Shiah, Hsu and Hwu (2018)]. Also in Eq. (7), m is an integer sufficiently large for series convergence; m=16 is quite enough for highly anisotropic properties. For evaluating the last integral in Eq. (6), one also needs the explicit expression of $G_{j,k}^*$, which can be obtained by directly differentiating Eq. (7) under the polar coordinate system to give

$$\begin{aligned} G_{j,1}^* = {} & 2\overline{\Re}_j^{(1)} \ln r + \left(2\overline{\Re}_j^{(1)} \cos^2\theta - \overline{\Im}_j^{(1)} \sin(2\theta) \right) \\ & + 2 \sum_{n=2}^{16} \begin{bmatrix} \overline{\Re}_j^{(n)} \left(\cos\theta \cos(n\theta) + n \sin\theta \sin(n\theta) \right) \\ -\overline{\Im}_j^{(n)} \left(\cos\theta \sin(n\theta) - n \sin\theta \cos(n\theta) \right) \end{bmatrix}, \end{aligned} \tag{8a}$$

$$\begin{aligned} G_{j,2}^* = {} & -2\overline{\Im}_j^{(1)} \ln r + \left(\overline{\Re}_j^{(1)} \sin(2\theta) - 2\overline{\Im}_j^{(1)} \sin^2\theta \right) \\ & + 2 \sum_{n=2}^{16} \begin{bmatrix} \overline{\Re}_j^{(n)} \left(\sin\theta \cos(n\theta) - n \cos\theta \sin(n\theta) \right) \\ -\overline{\Im}_j^{(n)} \left(\sin\theta \sin(n\theta) + n \cos\theta \cos(n\theta) \right) \end{bmatrix}. \end{aligned} \tag{8b}$$

It should be noted that solving the BIE in Eq. (7) neither relies on any coordinate transformation as presented in Eq. (5) nor requires any extra line integral as presented previously. Apparently, the BIE in Eq. (6) is much easier to be applied for solving the problem of anisotropic thermoelasticity.

3 Regularization of the BIE for analyzing thin layers

For analyzing interlaminar stresses in adjoined composites, the usual sub-regioning technique in the BEM can be applied, where an assemblage of combined matrices is built following the collocation process for each respective sub-domain, to solve for all boundary unknowns. Since this technique has been well established in the literature, no further explanations are provided here. However, there is a key issue to be addressed for analyzing thin composites, that is, the problem of "near-singularity". In modeling thin layers by the BEM, the source point on one side of a layer will be very near an

integration element on its opposite side. As is well known for the BEM modeling, this situation will cause sudden rise-ups of those integrands associated with r, the distance between P and Q. Under this circumference, any conventional integration scheme cannot properly yield reliable values unless the integral is "completely regularized". Due to its conciseness in form, our main task targets regularization of Eq. (6) rather than Eq. (5) for analyzing dissimilarly adjoined thin composites.

For performing the collocation process, the boundary is discretized into M quadratic elements. The discretized form of Eq. (6) is given by

$$C_{ij}u_i = \sum_{d=1}^{M}\sum_{c=1}^{3} {}^{d}t_i^{(c)} \int_{-1}^{1} U_{ij}^{*} N^{(c)}\, J\, d\xi - \sum_{d=1}^{M}\sum_{c=1}^{3} {}^{d}u_i^{(c)} \int_{-1}^{1} T_{ji}^{*} N^{(c)} J\, d\xi$$
$$+\mathrm{K}_{ik}\sum_{d=1}^{M}\sum_{c=1}^{3} {}^{d}\Phi^{(c)} \int_{-1}^{1} G_{j,k}^{*} N^{(c)} n_i J\, d\xi - \mathrm{K}_{ik}\sum_{d=1}^{M}\sum_{c=1}^{3} {}^{d}\Phi_{,i}^{(c)} \int_{-1}^{1} G_{j}^{*} N^{(c)} n_k J\, d\xi\,, \tag{9}$$

where J stands for the Jacobian of transformation from the Cartesian coordinates to the local coordinate ξ, and the superscripts d and (c) are used to denote nodal values of the c-th node on element d. On inspecting Eqs. (3a)-(3c), the fundamental solutions of U_{ij}^{*} and T_{ij}^{*} are characterized by the singular orders $O(\ln r)$ and $O(1/r)$, respectively. Regularizations for the first two boundary integrals in Eq. (6), containing U_{ij}^{*} or T_{ij}^{*} in the integrand, have been discussed with great details in Shiah et al. [Shiah, Hwu and Yao (2019)] and thus, only their final regularized expressions are reviewed here. As presented, the regularized form of the first two integrals are given by

$$\int_{-1}^{1} U_{ij}^{*} N^{(c)}\, J\, d\xi = 2\,\mathrm{Re}\left\{\alpha_{ik} B_{jk}\left[J\, v\, N^{(c)}\Big|_{-1}^{1} - \int_{-1}^{1} v\,\Omega^{(c)} d\xi\right]\right\}, \tag{10a}$$

$$\int_{-1}^{1} T_{ji}^{*} N^{(c)} J\, d\xi = (-1)^{i-1}\,\mathrm{Re}\left\{\left\langle \begin{array}{l} \dfrac{\mu_k^{\delta_{1i}} B_{jk}}{A_{1k}(R_{1k}-R_{2k})} + \\ \dfrac{\lambda^{(c)} V_k (R_{1k}-R_{2k})}{2}\xi^2 \\ \quad + \left[\begin{array}{l} V_k(S_{1k}-S_{2k}) \\ +\lambda^{(c)} H_k (R_{1k}-R_{2k}) \end{array}\right]\xi \\ +S_{1k}(H_k + R_{1k}V_k)\ln(\xi - R_{1k}) \\ -S_{2k}(H_k + R_{2k}V_k)\ln(\xi - R_{2k}) \end{array}\right\rangle\Bigg|_{-1}^{1}\right\}, \tag{10b}$$

where (k=1, 2) for summation has been omitted, R_{ik} are the polynomial roots of the radial distance function formulated in terms of ξ, and the explicit expressions of all other parameters in the above equations can be referred to Shiah et al. [Shiah, Hwu and Yao (2019)]. As derived in Shiah et al. [Shiah, Hwu and Yao (2019)], the integrand in Eq. (10a) is non-singular and all other terms in both Eqs. 10(a) and 10(b) can be evaluated

analytically. From Eq. (7), it is apparent that the integral associated with G_j^* is non-singular because its integrand converges under the condition when r approaches to null. Thus, the only task left for analyzing thin composites is to regularize the remaining integral in Eq. (9), namely

$$I_{ijk}^{(c)} = \int_{-1}^{1} G_{j,k}^* N^{(c)} n_i J \, d\xi. \tag{11}$$

On inspecting Eqs. 8(a) and 8(b), one may have the impression that only those terms with $\ln r$ need to regularization. However, it was found that the rest of the other integrals written in terms of θ would fluctuate rapidly but not in the same manner as we had known for near-singularity. Fig. 1 displays the variations of $\cos(10\theta)$ and $\cos(20\theta)$ of a typical case, for example, where the source point approaches the middle node of a straight element (length=l) at a distance r_0. From the figure, one may observe two phenomena-one is the presence of more ripples present in the function containing $\cos(n\theta)$ for greater n, and the other is the clustering of the ripples when the distance ratio is small. For these, proper numerical integration of the integral in Eq. (11) becomes an issue, not being featured totally by the near-singularity in convention.

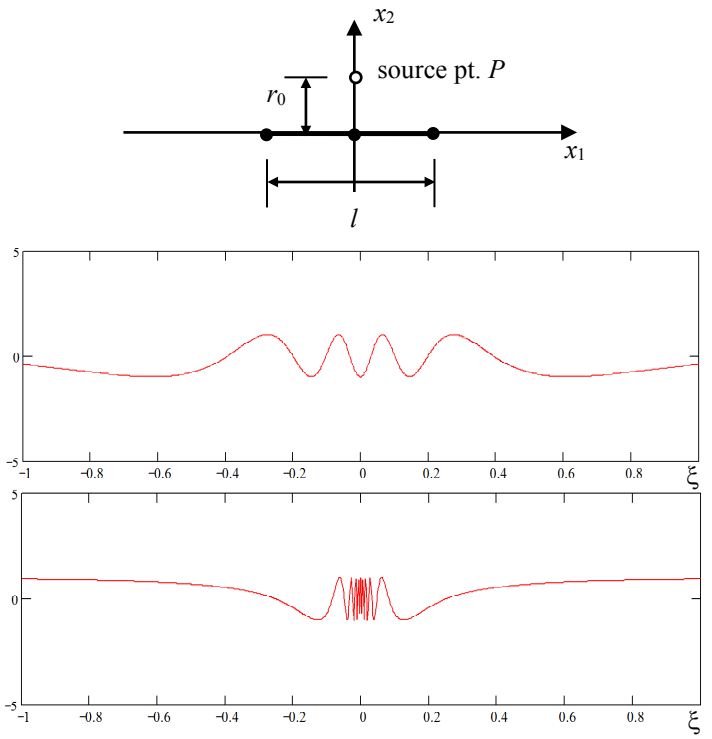

Figure 1: Fluctuations of $\cos(10\theta)$ and $\cos(20\theta)$ for a typical case

By substituting the expressions in Eq. (8), the quadratic shape functions, and those regarding the outward normal unit vector into Eq. (11), one obtains

$$I_{ij1}^{(c)} = (-1)^{i+1} 2\overline{\Re}_j^{(1)} \int_{-1}^{1} \ln r \cdot \left(\sum_{m=0}^{2} \overline{\eta}_{mi}^{(c)} \xi^m \right) d\xi$$
$$+(-1)^{i+1} 2 \int_{-1}^{1} \left(\overline{\Re}_j^{(1)} \cos^2\theta - \overline{\Im}_j^{(1)} \sin\theta\cos\theta \right) \left(\sum_{m=0}^{3} \overline{\eta}_{mi}^{(c)} \xi^m \right) d\xi \quad , \tag{12a}$$
$$+2(-1)^{i+1} \int_{-1}^{1} \sum_{n=2}^{16} \begin{bmatrix} \overline{\Re}_j^{(n)} \left(\cos\theta\cos n\theta + n\sin\theta\sin n\theta \right) \\ -\overline{\Im}_j^{(n)} \left(\cos\theta\sin n\theta - n\sin\theta\cos n\theta \right) \end{bmatrix} \left(\sum_{m=0}^{3} \overline{\eta}_{mi}^{(c)} \xi^m \right) d\xi$$

$$I_{ij2}^{(c)} = (-1)^{i} 2\overline{\Im}_j^{(1)} \int_{-1}^{1} \ln r \cdot \left(\sum_{m=0}^{2} \overline{\eta}_{mi}^{(c)} \xi^m \right) d\xi$$
$$+(-1)^{i+1} \int_{-1}^{1} \left(\overline{\Re}_j^{(1)} \sin 2\theta - 2\overline{\Im}_j^{(1)} \sin^2\theta \right) \left(\sum_{m=0}^{3} \overline{\eta}_{mi}^{(c)} \xi^m \right) d\xi \quad . \tag{12b}$$
$$+2(-1)^{i+1} \int_{-1}^{1} \sum_{n=2}^{16} \begin{bmatrix} \overline{\Re}_j^{(n)} \left(\sin\theta\cos n\theta - n\cos\theta\sin n\theta \right) \\ -\overline{\Im}_j^{(n)} \left(\sin\theta\sin n\theta + n\cos\theta\cos n\theta \right) \end{bmatrix} \left(\sum_{m=0}^{3} \overline{\eta}_{mi}^{(c)} \xi^m \right) d\xi$$

where the coefficients $\overline{\eta}_{mi}^{(c)}$ can be readily formulated in terms of the coefficients of ξ^m of the c-th shape functions as well as the nodal coordinates $x_i^{(c)}$ of the integration element and thus, their very explicit expressions will not be elaborated tediously here. As explained earlier, the nature of near-singularity is seen in the first integral in Eqs. 12(a) and (12b); however, another difficulty of numerical integration is present due to the rapid fluctuations in integrands of the rest of the integrals. In what follows, these issues will be resolved step by step. The first integral is characterized by the singular order $O(\ln r)$, which can be rewritten as follows:

$$\int_{-1}^{1} \ln r \cdot \left(\sum_{m=0}^{2} \overline{\eta}_{mi}^{(c)} \xi^m \right) d\xi = \frac{\lambda_4}{2} \sum_{k=1}^{4} \sum_{m=0}^{2} \overline{\eta}_{mi}^{(c)} \int_{-1}^{1} \xi^m \cdot \ln\left(\xi - \varpi_k \right) d\xi \,, \tag{13}$$

where ϖ_k are complex roots of a quartic polynomial, formulated by interpolation of the Cartesian coordinates in the radial distance, and λ_4 is the non-zero coefficient of ξ^4. It should be noted that Eq. (13) is formulated especially for a general quadratic curved element, where λ_4 cannot be null (for a straight element). For the degenerate case when the constant λ_4 vanishes, the polynomial of the distance function will be quadratic and its similar derivation is even much simpler. Since the derivation can be readily made in a very similar manner, it will not be tediously elaborated here. Also, it is worth mentioning that when the point P is very near the integration element with projection point ξ_0, two of the conjugate roots will be very close to ξ_0 with their imaginary parts almost vanishing (near zero). After performing analytical integration of Eq. (13), one immediately obtains

$$\int_{-1}^{1} \ln r \cdot \left(\sum_{m=0}^{2} \overline{\eta}_{mi}^{(c)} \xi^m \right) d\xi$$

$$= \frac{\lambda_4}{72} \sum_{k=1}^{4} \left(\xi - \varpi_k \right) \left\{ \begin{array}{l} 6\ln(\xi - \varpi_k) \left[\begin{array}{l} 2\overline{\eta}_{2i}^{(c)} \left(\varpi_k^2 + \varpi_k \xi + \xi^2 \right) \\ +3\overline{\eta}_{1i}^{(c)} \left(\varpi_k + \xi \right) + 6\overline{\eta}_{0i}^{(c)} \end{array} \right] \\ -2\overline{\eta}_{2i}^{(c)} \left(11\varpi_k^2 + 5\varpi_k \xi + 2\xi^2 \right) \\ -\overline{\eta}_{1i}^{(c)} \left(27\varpi_k + 9\xi \right) - 36\eta_0 \end{array} \right\} \Bigg|_{-1}^{1} . \tag{14}$$

Now, correct evaluations of Eqs. 12(a) and 12(b) totally rely on the regularization of the other integrals, represented by

$$\int_{-1}^{1} F_{ij}(\theta) \cdot \left(\sum_{m=0}^{3} \overline{\eta}_{mi}^{(c)} \xi^m \right) d\xi = \sum_{m=0}^{3} \overline{\eta}_{mi}^{(c)} \cdot D_{ij}^{(m)} , \tag{15}$$

where $F_{ij}(\theta)$ stands for the θ-function in the integrands of Eqs. 12(a) and 12(b) and $D_{ij}^{(m)}$ is defined by

$$D_{ij}^{(m)} = \int_{-1}^{1} F_{ij}(\theta) \cdot \xi^m \, d\xi, \ (m = 0, 1, 2, 3) . \tag{16}$$

Obviously, analytical integration of Eq. (16) appears not so feasible due to the mathematical complexity of $F_{ij}(\theta)$.

As elucidated earlier, the drastic fluctuation of $F_{ij}(\theta)$ for very small r will pose difficulties in numerical integration. This is because of the fact that $d\xi$ in the local coordinate shall give rise to rapid variation of θ and the trigonometric functions cos($n\theta$) and sin($n\theta$) even make the variation more drastic for large n when the source point is very near the integration element. Fortunately, this issue is not as serious as that of the near-singularity. For resolving this issue, three approaches by the Gauss quadratic rule can be applied, namely (A) Taking more Gauss points, (B) Making ξ-θ variable transformation, and (C) Performing separate integration in sub-regions. For applying (A), very large numbers of integration points are required for treating very thin layers and no accuracy can be guaranteed for a certain number of Gauss points if the thickness order is very small as compared with the domain's characteristic dimension. For applying (B), the following variable transformation is firstly carried out,

$$\xi = \frac{\Delta x_2 \cos\theta - \Delta x_1 \sin\theta \pm \sqrt{\begin{array}{l} \left(\Delta x_2 \cos\theta - \Delta x_1 \sin\theta \right)^2 \\ -16 \left(\delta x_2 \cos\theta - \delta x_1 \sin\theta \right) \left(Dxp_2 \cos\theta - Dxp_1 \sin\theta \right) \end{array}}}{\left(\delta x_2 \cos\theta - \delta x_1 \sin\theta \right)} , \tag{17}$$

where the constants Δx_i and δx_i are defined by nodal coordinates of the c-th node of a quadratic element (c=1, 2, 3), denoted by $x_i^{(c)}$ and Dxp_i is associated with the field point, denoted by xp_i; they are given as follows:

$$\Delta x_i = x_i^{(3)} - x_i^{(1)}, \quad \delta x_i = 2x_i^{(3)} - 4x_i^{(2)} + 2x_i^{(1)}, \quad Dxp_i = x_i^{(2)} - xp_i \,. \tag{18}$$

It should be noted that Eq. (17) is a general form for curved elements when $\delta x_i \neq 0$ and formulation for the degenerate case of straight elements needs to be re-derived. Since the derivation for straight elements is much simpler, no further discussions will be addressed for the degenerate case. By directly differentiating Eq. (17), one may readily obtain $d\xi/d\theta$ expressed as function of θ for the general case of a curved element. Using this transformation, Eq. (16) may be integrated in a usual manner. This approach may help relax fluctuations of the integrands; however, increased numbers of Gauss points are still needed for acquiring integration accuracy. The last approach, i.e., method (C), is simply to divide the integration domain into sub-regions as follows:

$$D_{ij}^{(m)} = \int_{-1}^{\xi_0-\delta} F_{ij}(\theta)\cdot\xi^m \, d\xi + \int_{\xi_0-\delta}^{\xi_0+\delta} F_{ij}(\theta)\cdot\xi^m \, d\xi + \int_{\xi_0+\delta}^{1} F_{ij}(\theta)\cdot\xi^m \, d\xi \,, \tag{19}$$

where ξ_0 is the local coordinate of the projection point on the integration element and δ is a small interval. One may only slightly increase the number of Gauss points for the integration in the neighborhood of ξ_0, while the other integrals can be integrated with a few Gauss points in a usual manner.

The three approaches were tested for their accuracies by investigating a typical example that the nodal coordinates of an arc element and the source point are defined by:

$$\begin{aligned} &x_1^{(1)} = \cos(\pi/6), \quad x_1^{(2)} = \cos(\pi/4), \quad x_1^{(3)} = \cos(\pi/3), \\ &x_2^{(1)} = \sin(\pi/6), \quad x_2^{(2)} = \sin(\pi/4), \quad x_2^{(3)} = \sin(\pi/3), \\ &xp_1 = (1-d)\cos(\pi/3.8), \quad xp_2 = (1-d)\sin(\pi/3.8), \end{aligned} \tag{20}$$

where d is the radial distance between point P and the arc element for integration. For the numerical test, integration was performed by the Gauss quadrature rule for the following integral,

$$I = \int_{-1}^{1} \cos\theta \cdot \cos(20\theta)\cdot\xi \, d\xi \,. \tag{21}$$

For this integration element with arc length L=π/3, one may calculate Eq. (21) by the three approaches for various distance ratios, ζ=d/L, to test the computational accuracy as compared with the results computed by MathCAD, commercial software using the adaptive integration scheme.

It should be noted that the fluctuation will be less drastic when the power of ξ in the integrand is greater than one, and so is it for cos($n\theta$) when n is small. The reason of selecting this typical example is that its numerical integration is very sensitive for small d and all the terms in $D_{ij}^{(m)}$ appear less fluctuating than that in I. Tab. 1 lists the numerical results obtained by the three methods in comparison with those calculated by MathCAD,

commercial mathematical software. In the approach (C), increased Gauss points were only used for integrating the sub-domain including the projection point ξ_0, while the others were integrated simply by 8 Gauss points. A few conclusions can be drawn from the test. Firstly, method (A) using large numbers of Gauss points cannot efficiently acquire computation accuracy for small ζ. Secondly, method (B) can increase the computation accuracy when the number of Gauss points is increased; however, the gain may not deserve the extra computational costs due to the mathematical complexity of the integrand. At last, method (C) can efficiently increase the accuracy for very small ζ by simply using 8 Gauss points when proper δ is selected. Hence, the method (C) is employed for implementation in the BEM as presented in the following numerical examples.

Table 1: Integration results by different methods (A), (B), and (C) for the test example

d/L	Math CAD	Gauss no.	(A) (% Diff.)	(B) (% Diff.)	(C) (% Diff.)	
					δ	
10^0	-0.10404	8	-0.10667 (2.53%)	-0.10447 (0.41%)	0.250	-0.10404 (0.00%)
		16	-0.10404 (0.00%)	-0.10404 (0.00%)		-0.10404 (0.00%)
10^{-1}	-0.17905	8	-0.20586 (14.98%)	-0.33224 (85.56%)	0.250	-0.18005 (0.56%)
		16	-0.20120 (12.37%)	-0.16665 (6.92%)		-0.17747 (0.88%)
10^{-2}	0.14129	8	0.15359 (8.70%)	0.45376 (221.15%)	0.055	0.14183 (0.38%)
		16	0.10850 (23.21%)	0.16412 (16.16%)		0.13917 (1.50%)
10^{-3}	-0.09532	8	-0.08475 (11.09%)	0.25901 (372.02%)	0.020	-0.09519 (0.14%)
		16	-0.09829 (3.11%)	-0.03353 (64.78%)		-0.09488 (0.46%)
10^{-4}	-0.13712	8	-0.11279 (17.74%)	0.23259 (269.59%)	0.020	-0.13699 (0.10%)
		16	-0.14283 (4.16%)	-0.05276 (61.53%)		-0.13690 (0.16%)
10^{-5}	-0.14328	8	-0.12119 (15.42%)	0.22971 (260.25%)	0.020	-0.14323 (0.03%)
		16	-0.14723 (2.76%)	-0.05181 (63.86%)		-0.14331 (0.02%)

4 Illustrative examples

All formulations presented previously for quadratic isoparametric elements have been programmed in an existing code, developed by FORTRAN. To illustrate the veracity of the implemented code, a few numerical examples are analyzed by both of the present BEM approach as well as the finite element method by ANSYS. Quartz was selected as the material for the analysis of all examples, which has the following properties (defined by their conventional symbolic notations):

$$E_{11}^{*}=34.50\,\text{GPa},\ E_{22}^{*}=51.60\,\text{GPa},\ E_{33}^{*}=25.00\,\text{GPa},\ G_{12}^{*}=3.70\,\text{GPa},\ G_{23}^{*}=54.0\,\text{GPa},$$
$$G_{31}^{*}=6.30\,\text{GPa},\ \nu_{12}^{*}=0.28,\ \nu_{13}^{*}=0.34,\ \nu_{23}^{*}=0.28,\ \eta_{12,1}^{*}=0,$$
$$\eta_{12,2}^{*}=0,\ \eta_{12,3}^{*}=0,\ \mu_{31,23}^{*}=0.0\ , \tag{22}$$

where the asterisk mark is to denote properties defined by the material's principal axes. The thermal expansion coefficients α_{ij}^{*} and the conductivities for the analysis are

$$\alpha_{11}^{*}=2.8\times10^{-6}\ (1/^{\circ}C),\alpha_{22}^{*}=9.0\times10^{-6}\ (1/^{\circ}C),$$
$$\alpha_{33}^{*}=3.4\times10^{-6}\ (1/^{\circ}C),\mathrm{K}_{11}^{*}=4.18\ (W/m^{\circ}C),\ \mathrm{K}_{22}^{*}=4.98\ (W/m^{\circ}C). \tag{23}$$

Epoxy was selected to be the adhesive material, which has the following properties:

$$E=20.7\,\text{GPa},\ G=8.28\,\text{GPa},\ \nu=0.25,\ \alpha=3.0\times10^{-6}(1/^{\circ}C),\ \mathrm{K}=1.26(W/m^{\circ}C). \tag{24}$$

4.1 Example I

Shown in Fig. 2 is the 1st example, treating a composite with three thin layers of quartz (denoted respectively by Quartzs 1-3 from bottom to top) bonded together by epoxy. The dimension of each quartz layer is 1 (m)×0.012 (m) and the thickness of each adhesive layer is assumed to be 2 (mm). For yielding generally anisotropic properties, the principal axes are arbitrarily rotated by 30°, 45°, and 60° counterclockwise for Quartzs 1, 2, and 3, respectively. For prescribing boundary conditions, all surfaces are retrained from moving in the normal directions and free to move in their tangential directions. The left and right sides are subjected to 0°C and 100°C respectively, and the other two opposite surfaces are insulated. As aforementioned, due to the modeling difficulties, modeling of very thin layers is usually omitted in the conventional analysis. To investigate whether such omitting is meaningful or not, the simplified model without the thin adhesive layers was also analyzed. As shown in Fig. 2 for the BEM modeling, total 170 elements were employed to model the whole 5 layers of the former case, while only 72 elements were used to model the latter when no adhesive layers are present. As an independent verification tool, the FEM software ANSYS was also employed for the analysis of the both cases.

Fig. 3 plots the distributions of the total displacement U_t ($=\sqrt{u_1^2+u_2^2}$) of the interfaces, normalized by the factor $L\alpha_{11}^{*}\Delta\phi$ ($\Delta\phi$=100°C). As can be seen from the plots, all displacement solutions of the BEM analysis using the regularized boundary integral equation agree fairly well with those calculated by ANSYS. Another interesting

phenomenon observed is the difference of the both analyses for 5 layers and 3 layers. Displacements on interface I_1 of the former case are generally smaller than those of the latter. However, the results on interface I_2 in the 1st case with epoxy are greater than those in the 2nd one for $x_1/L<0.375$ roughly and thereafter, the trend starts to reverse to the right end.

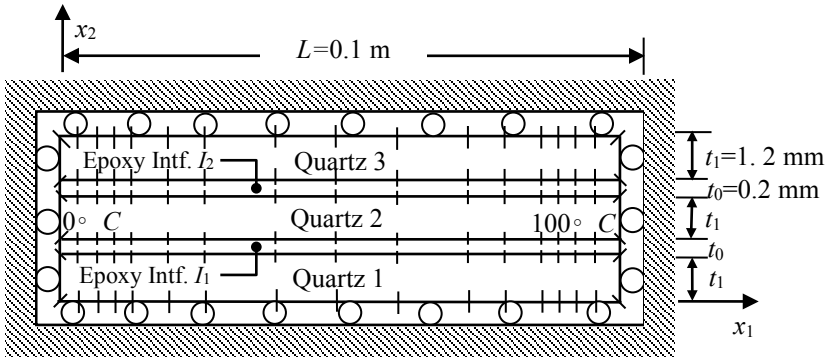

(Not drawn to scale)

Figure 2: Thin quartz layers bonded with epoxy

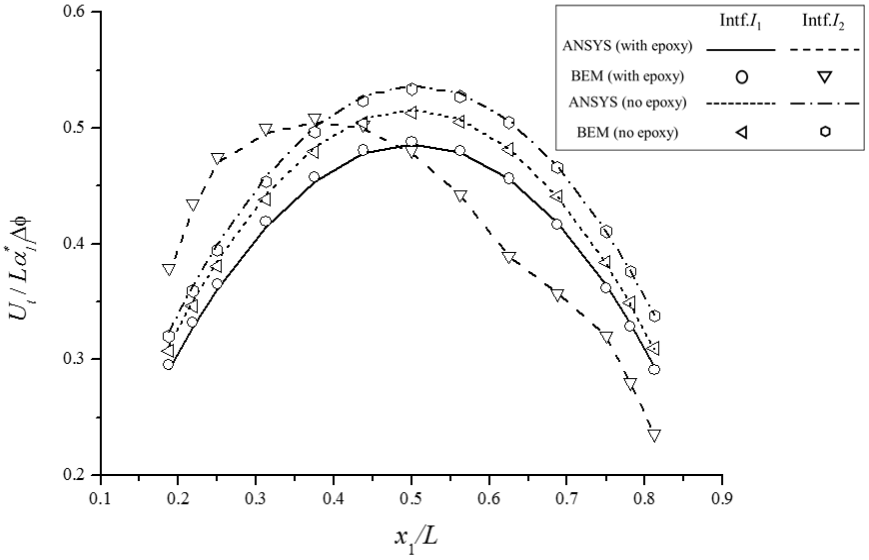

Figure 3: Distributin of the normalized total displacement along interfaces-*Example I*

Because all sides are constrained in their normal directions, σ_{11} and σ_{22} dominate the stress distributions on interfaces when other shears are negligible. Figs. 4, 5 plot the distribution of σ_{11} along interfaces for the both Cases of 3 and 5 layers, respectively. As can be observed from the figures, the compressive stresses σ_{11} in the interfaces of 3 layers (without epoxy) are generally greater than those of 5 layers (with epoxy). In either

case, the stresses on I_2 are comparatively larger than those on I_1. Consistently, the compressive stresses of Quartz 2 are larger than those of Quartz 1 on the both interfaces.

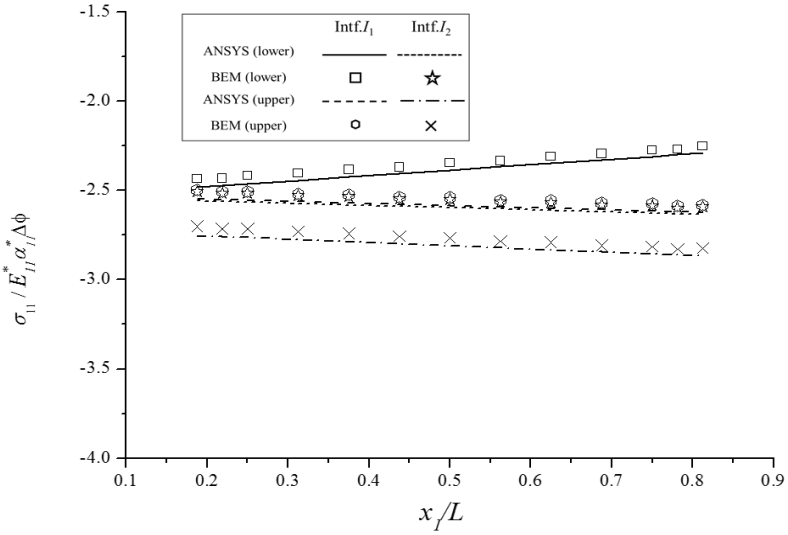

Figure 4: Distribution of normalized σ_{11} on interfaces of 3 layers- *Example I*

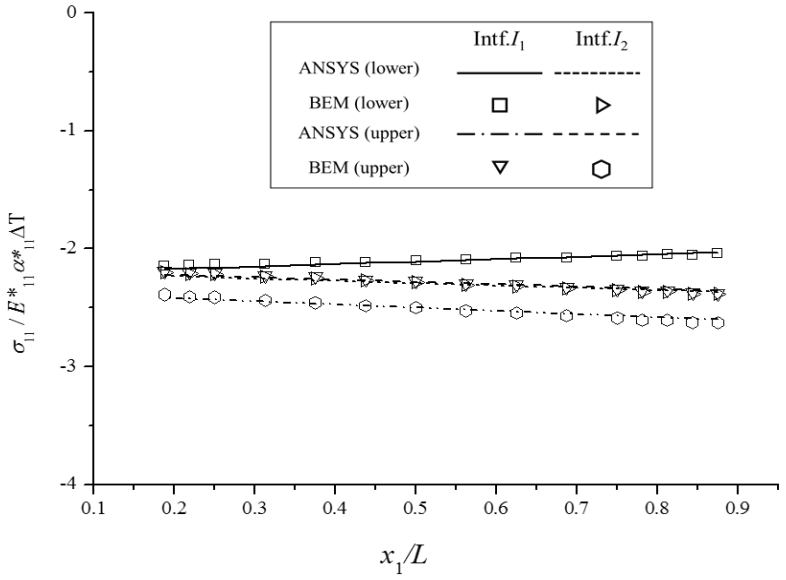

Figure 5: Distribution of normalized σ_{11} on interfaces of 5 layers- *Example I*

The similar comparison can be made for the distribution of σ_{22} on interfaces, which are shown in Figs. 6 and 7 for the both Cases of 3 and 5 layers, respectively. It is seen that the distributions of σ_{22} for the both cases are pretty close to each other. This phenomenon is due to the small dimension of each layer in the x_2 direction. Particularly, another

important analysis is for the stress distribution of the adhesive (epoxy) on interfaces, where potential debonding may occur.

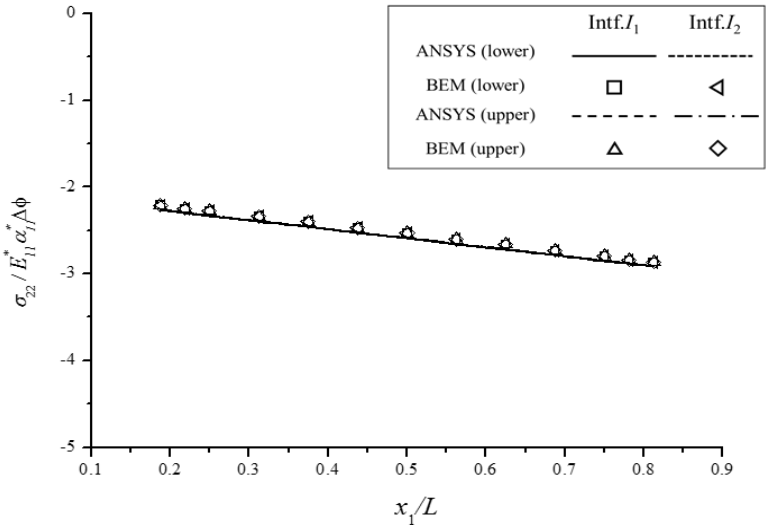

Figure 6: Distribution of normalized σ_{22} on interfaces of 3 layers- *Example I*

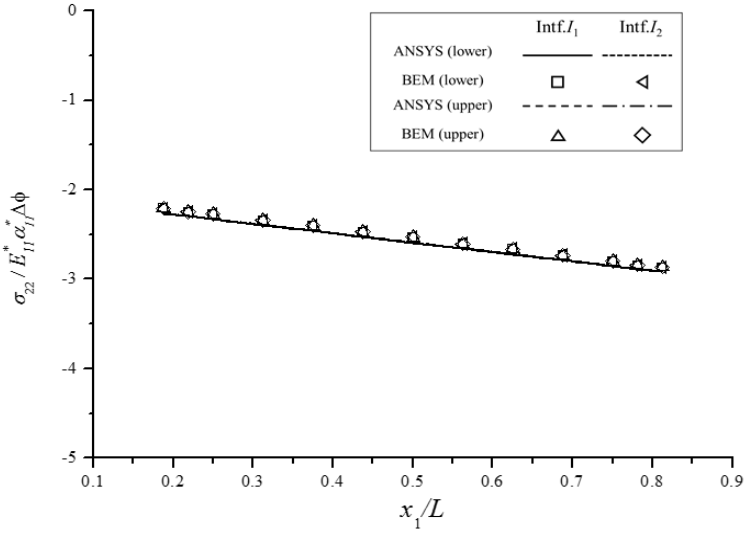

Figure 7: Distribution of normalized σ_{22} on interfaces of 5 layers- *Example I*

Distributions of the normalized dominant stresses, σ_{11} and σ_{22}, are plotted in Figs. 8 and 9, respectively. As can be observed from the figures, magnitude of the compressive stress σ_{11} is decreasing from the left end toward the right, whereas σ_{22} is distributed with the

opposite trend. In either distribution, both interfaces I_1, I_2 have pretty close stress values as can be expected due to the thinness of all epoxy layers. From all stress comparisons in Figs. 4-9, the BEM results agree pretty well with the FEM analyses.

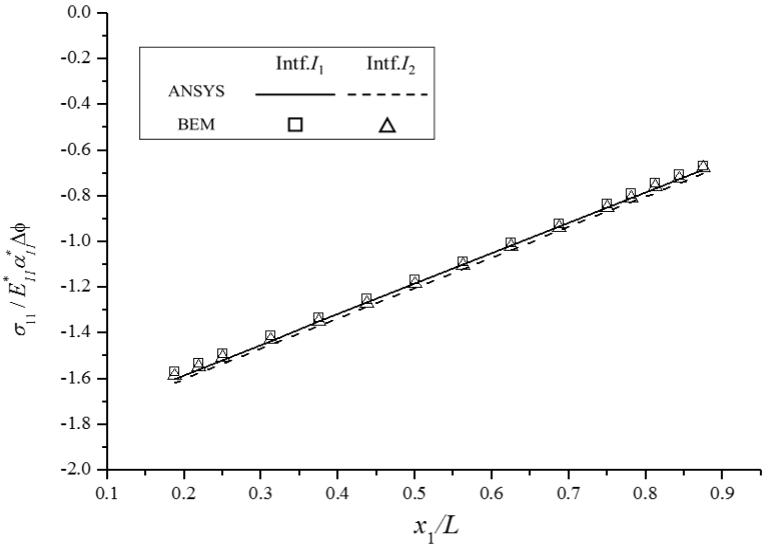

Figure 8: Distribution of normalized σ_{11} of epoxy in 5 layers- *Example I*

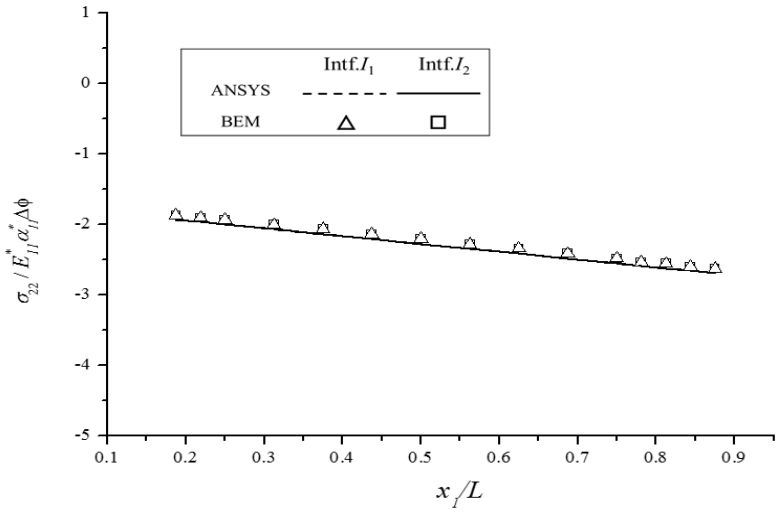

Figure 9: Distribution of normalized σ_{22} of epoxy in 5 layers- *Example I*

As aforementioned, conventional modeling of thin composites usually neglects the presence of thin adhesive layers due to modeling difficulties. For getting insight into the

necessity of modeling thin adhesive layers, comparisons of the equivalent stresses on interfaces of both 3 and 5 layers. The comparison for the interface I_1 is plotted in Fig. 10, showing the equivalent stresses for the three-layered case (without epoxy) are greater than those for the five-layered case (with epoxy). In a similar manner, the normalized σ_0 on the interface I_2 is plotted in Fig. 11, also showing the same trend as I_1.

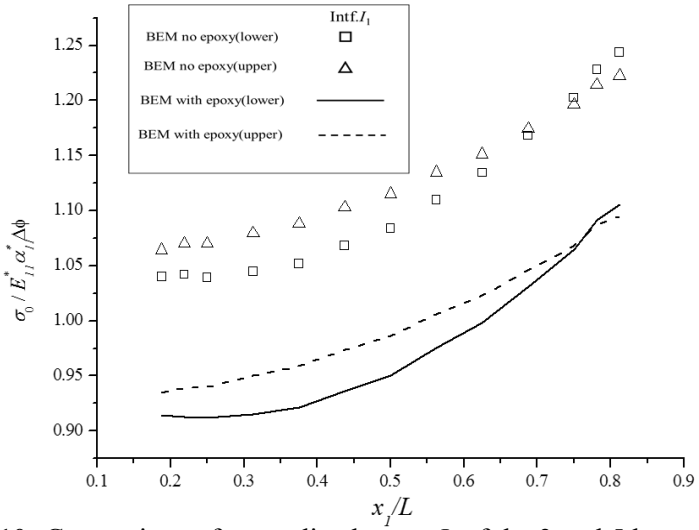

Figure 10: Comparison of normalized σ_0 on I_1 of the 3 and 5 layers- *Example I*

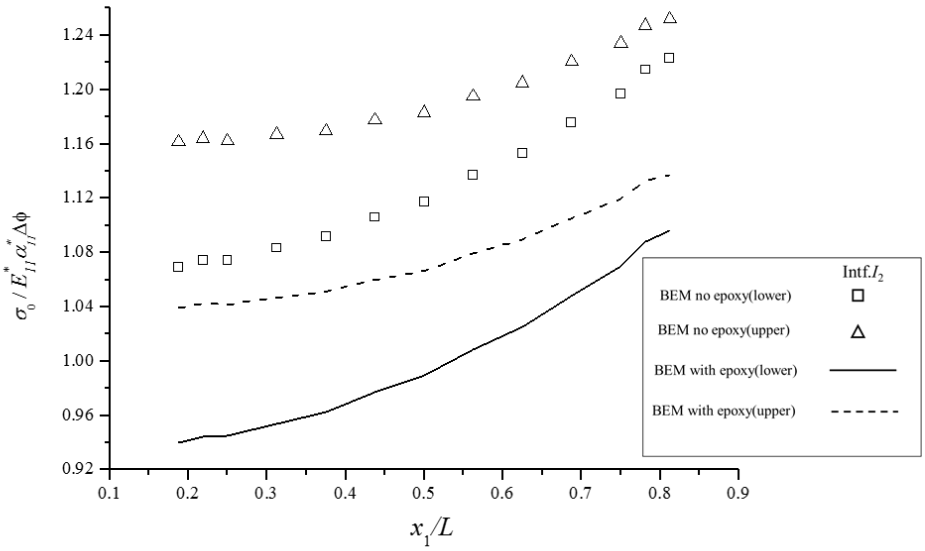

Figure 11: Comparison of normalized σ_0 on I_2 of the 3 and 5 layers- *Example I*

4.2 Example II

As another illustration of our BEM implementation, the second example treats a concentric quartz composite with inner radius L=10 (cm). The composite is made of three layers of different-phased quartz (denoted by Quartzs 1-3) bonded by thin layers of epoxy and thus, there are 5 layers in all as shown in Fig. 12. For giving generally anisotropic properties, the principal axes of Quartzs 1-3 are arbitrarily rotated counterclockwise by 10°, 50°, and 70°, respectively. Each quartz layer has thickness 0.015 (cm) and the adhesive is also epoxy with thickness 0.004 (cm). The boundary conditions considers the outside surface fully constrained in all directions and the heat flux is initiated from the inner surface prescribed with 100°C flowing toward the outside surface maintained at 0°C. As in the previous example, the analysis is to make comparison of the two respective situations- one with thin adhesive and the other without. For the former case with 5 layers, the BEM modeling employed 320 quadratic elements; for the latter, only 192 elements were applied. Due to the thinness of the adhesive, all calculated values of displacements/stresses on both (inner and outer) interfaces of each epoxy layer are almost identical. Fig. 13 plots the total displacements on the interfaces I_1 and I_2, normalized by a factor $L\alpha_{11}^{*}\Delta\phi$ ($\Delta\phi$=100°C). As expected, displacements on I_1 are always greater than those on I_2 because of higher temperature on I_1. Another interesting phenomenon observed is the fact that the displacements on the interfaces of 3 layers (without epoxy) are greater than those of the other case when epoxy is applied on interface I_1; however, no certain trend is present for the other interface. As can be seen in Fig. 13, the computed displacements of the both cases agree between the BEM and FEM analyses. The computed σ_{11} for the both cases of 3 layers and 5 layers are plotted in Figs. 14 and 15, respectively. Comparisons of all other stress components can be seen in Figs. 16 and 17 for the distribution of normalized σ_{22} and Figs. 18 and 19 for normalized σ_{12}. Obviously, fairly good agreements of the BEM results with our FEM analyses are present for all stress components.

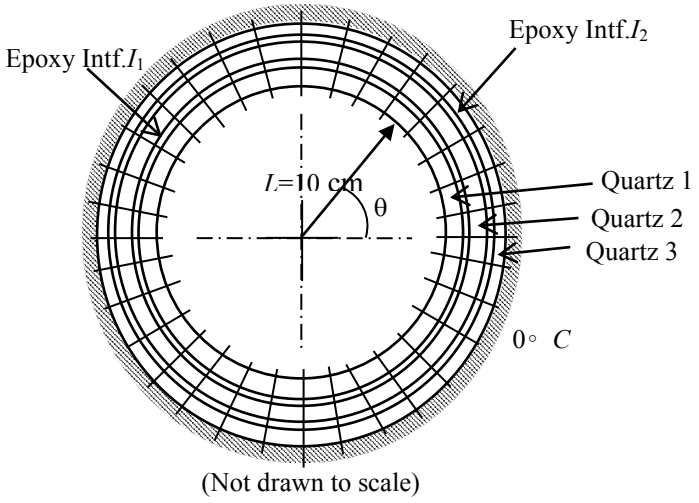

Figure 12: A concentric quartz composite subjected to thermal load- *Example II*

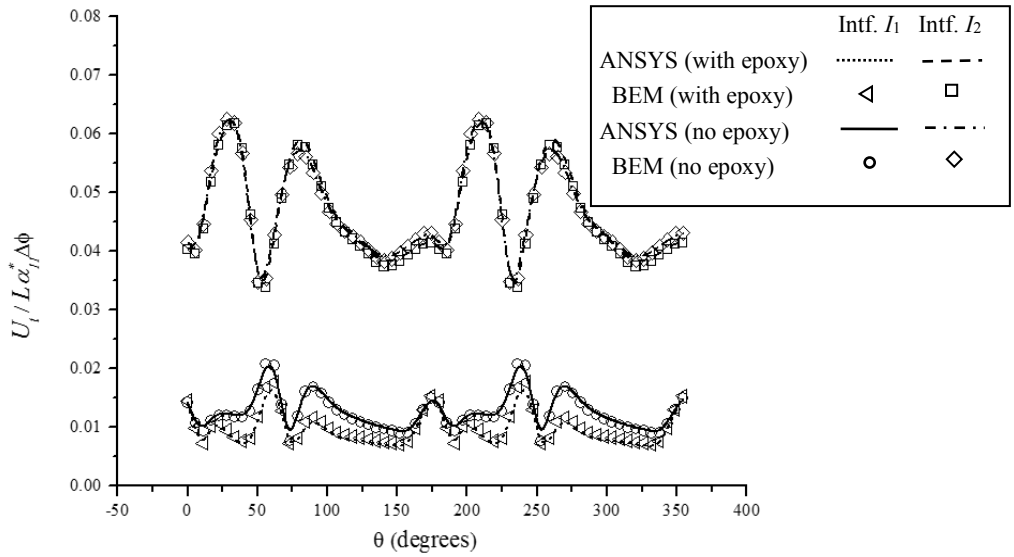

Figure 13: Distributin of the normalized total displacement along interfaces- *Example II*

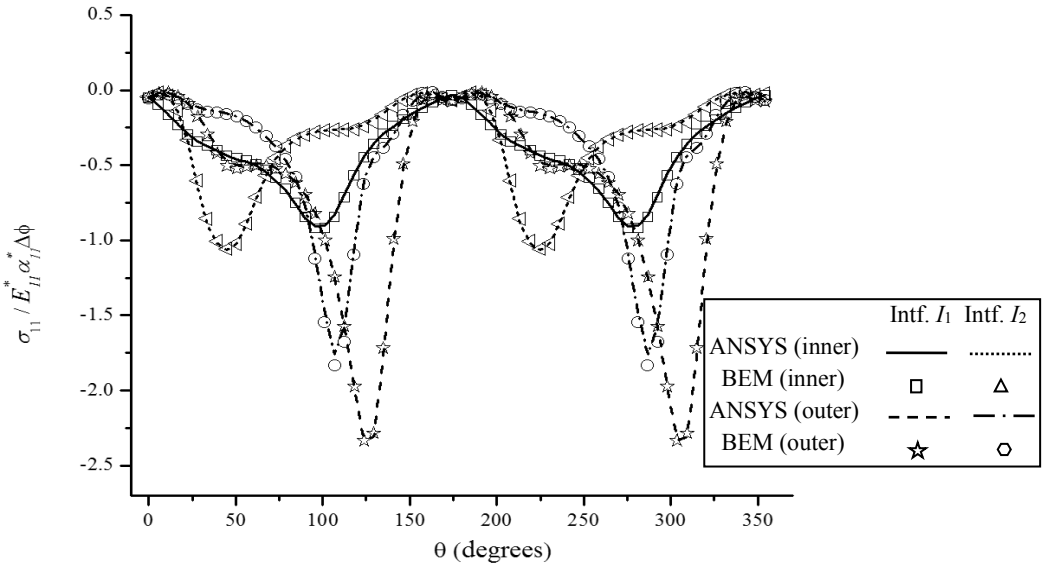

Figure 14: Distribution of normalized σ_{11} on interfaces of 3 layers- *Example II*

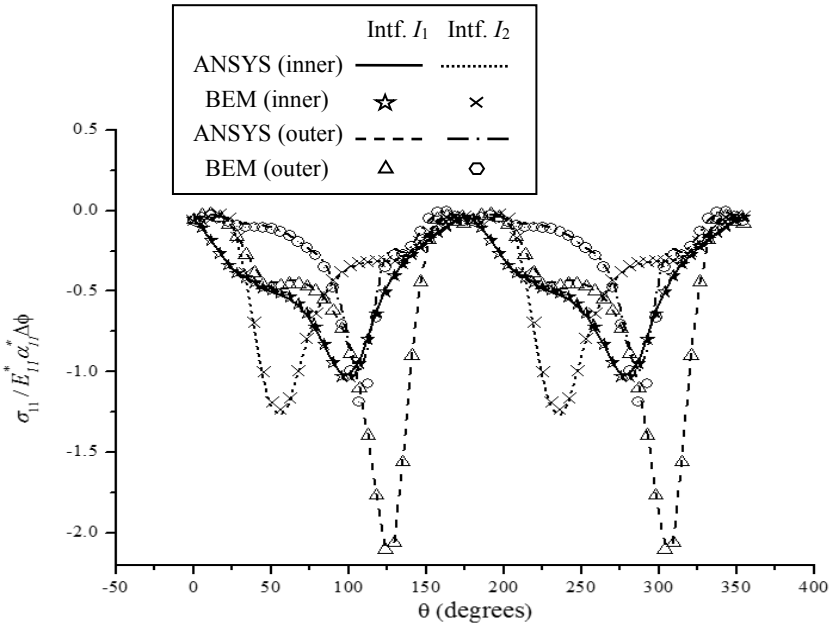

Figure 15: Distribution of normalized σ_{11} on interfaces of 5 layers- *Example II*

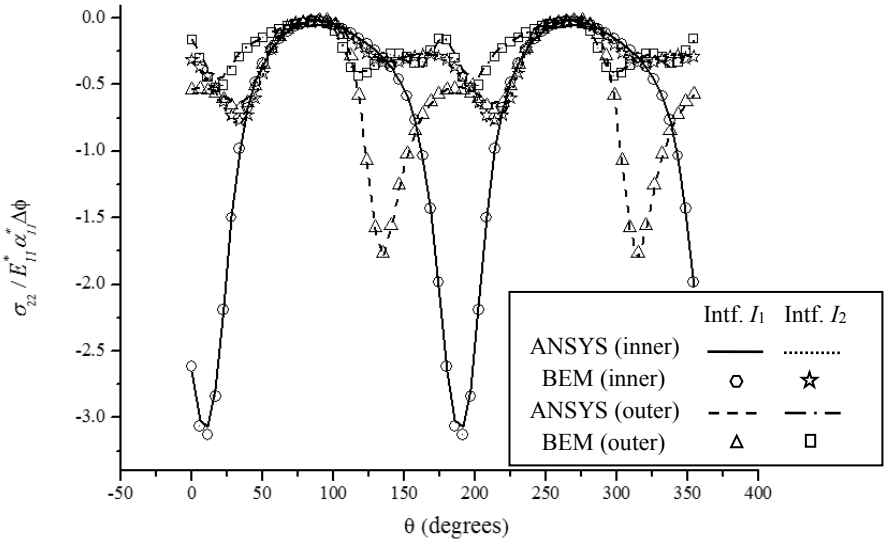

Figure 16: Distribution of normalized σ_{22} on interfaces of 3 layers- *Example II*

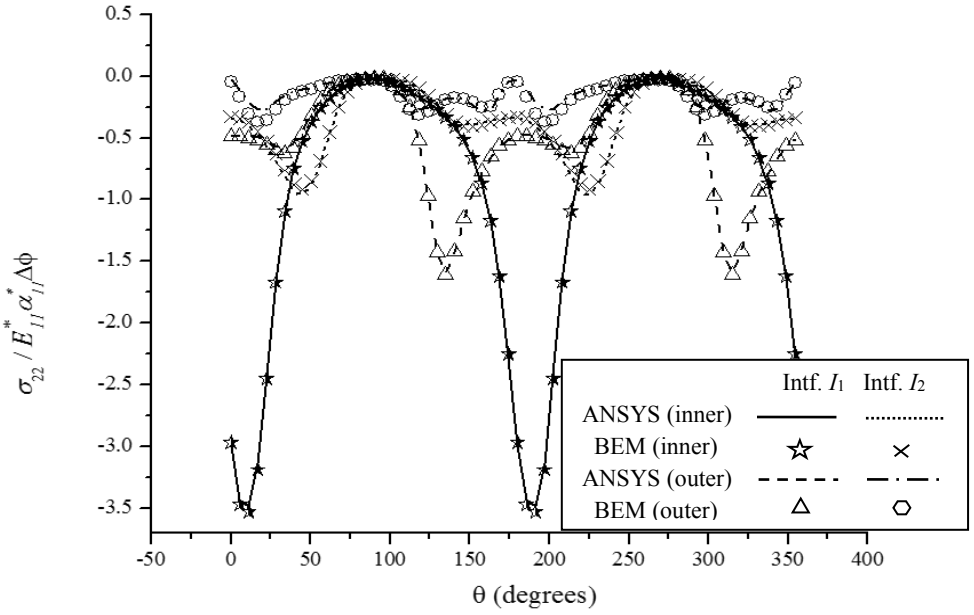

Figure 17: Distribution of normalized σ_{22} on interfaces of 5 layers- *Example II*

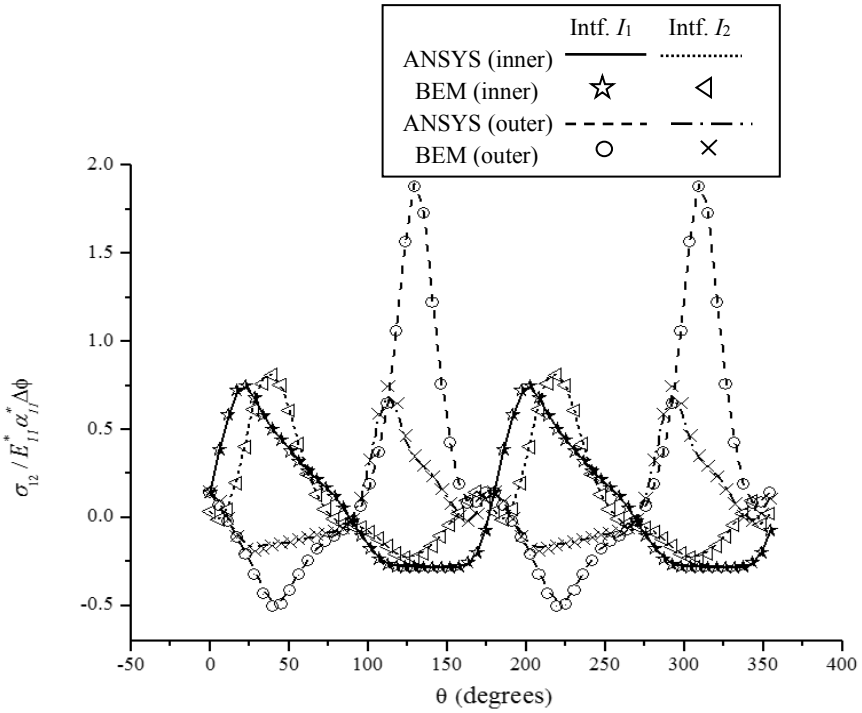

Figure 18: Distribution of normalized σ_{12} on interfaces of 3 layers- *Example II*

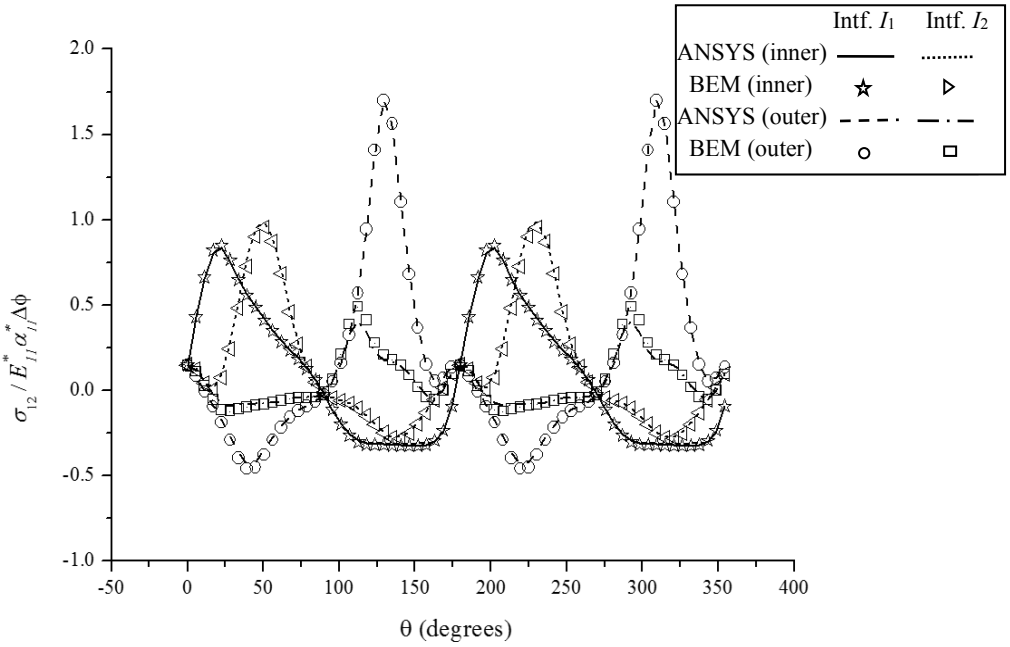

Figure 19: Distribution of normalized σ_{12} on interfaces of 5 layers-*Example II*

For assessing potential debonding, analyses for the thin epoxy layers play a crucial role. Fig. 20 plots the normalized total displacements of the epoxy on interface I_1 and I_2. Comparisons for all stress components σ_{11}, σ_{22}, and σ_{12} of the epoxy are plotted in Figs. 21-23, respectively. Once again, all BEM results agree well with the FEM analyses. It is interesting to observe that the normal stresses on I_1 are generally greater than those on I_2; however, no similar pattern is revealed for the shear. The equivalent stresses are also calculated for the interfaces in the both cases of three layers (without epoxy) and five layers (with epoxy) as displayed in Figs. 24 and 25 for I_1 and I_2, respectively. Interestingly, the fact is revealed that on the both interfaces, the equivalent stresses on the inner surface of quartz with epoxy layers are greater than those of the case when no epoxy is applied; however, this trend is reverse for the outer surfaces of the same interfaces of quartz.

5 Conclusions

On the use of bonded composites, one of the most concerned issues is the potential debonding that occurs at interfaces. However, due to the modeling difficulties of thin adhesives, conventional analyses usually neglect the presence of very thin adhesive layers. Indeed, such neglect has placed a risk of debonding at adhesives, leading to failure of the composites. In this paper, the BEM is employed to analyze the interfacial thermal stresses of dissimilarly adjoined thin anisotropic layers in two dimensions. For analysis of thin media, the boundary integral equation for anisotropic thermoelastic analysis is fully regularized such that only coarse meshes are required for yielding reliable results.

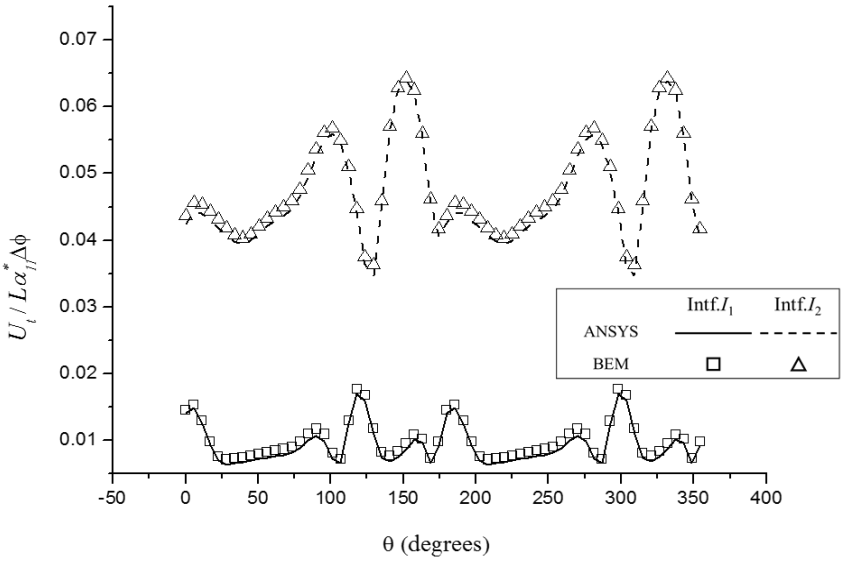

Figure 20: Distribution of normalized U_t of epoxy in 5 layers- *Example II*

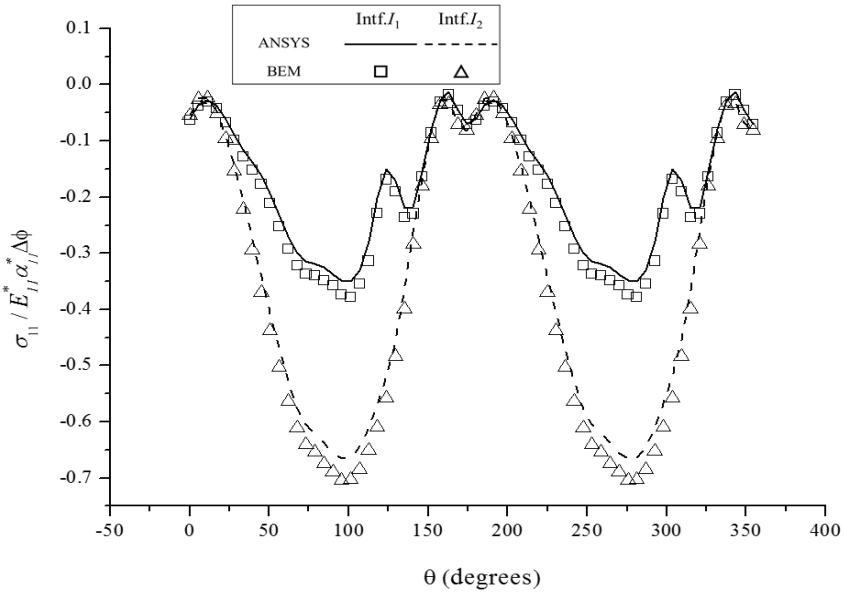

Figure 21: Distribution of normalized σ_{11} of epoxy in 5 layers- *Example II*

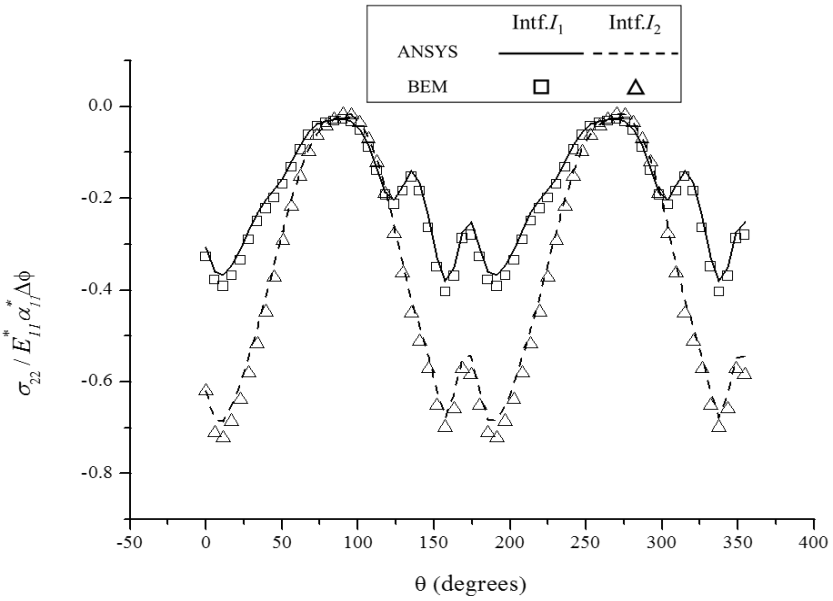

Figure 22: Distribution of normalized σ_{22} of epoxy in 5 layers- *Example II*

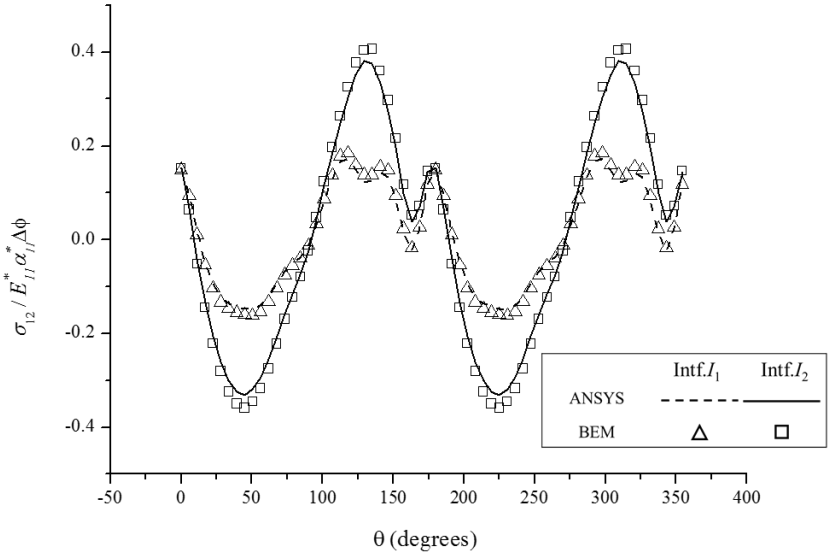

Figure 23: Distribution of normalized σ_{12} of epoxy in 5 layers- *Example II*

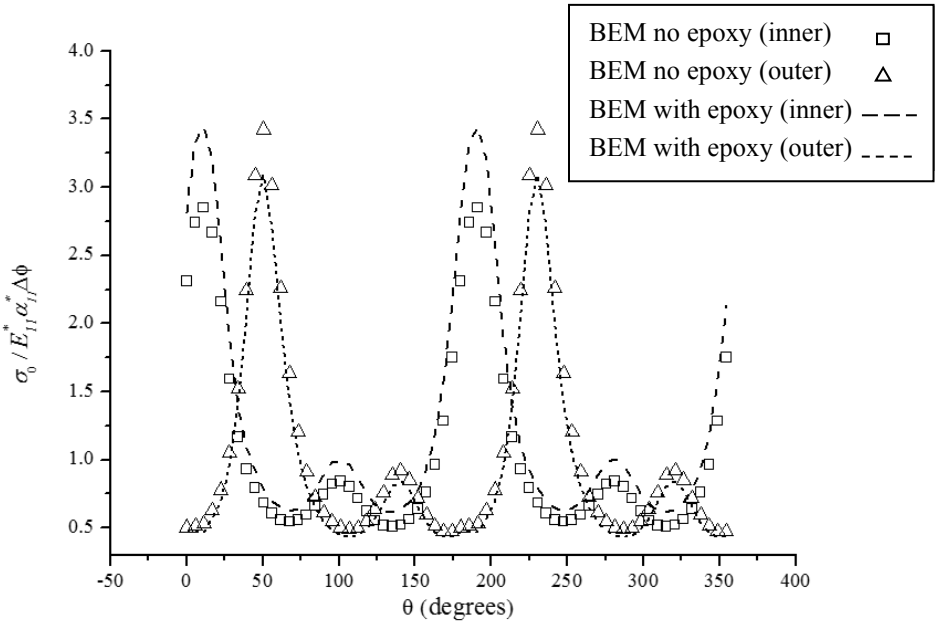

Figure 24: Comparison of normalized σ_0 on I_1 of the 3 and 5 layers

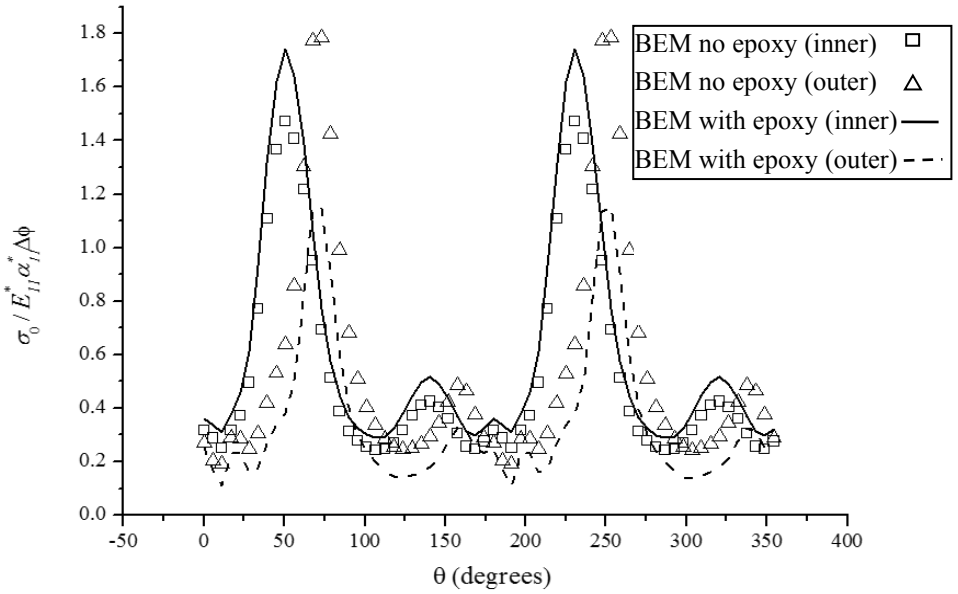

Figure 25: Comparison of normalized σ_0 on I_2 of the 3 and 5 layers

Truly, this regularized BIE is the first work presented for treating thin anisotropic composites, subjected to general thermal loads. All formulations have been implemented

in the BEM. Since the conventional analysis usually neglect the presence of thin adhesives, the present study has applied the implemented code to investigate the both cases when thin adhesive layers are neglected or considered. Comparisons are made for interfacial stresses of two benchmark examples of three and five layered composites. As a conclusion, evaluation of the adhesive layers is a must for assessing the structural integrity of composites and thus, the present work has truly laid a useful platform to ensure safe use of thin composites subjected to thermal loads.

Funding Statement: The financial support provided from the Ministry of Science and Technology of Taiwan is greatly appreciated by the authors (MOST 108-2221-E-006-186).

Conflicts of Interest: The authors declare that they have no conflicts of interest to report regarding the present study.

References

Bian, L. C.; Liu, W.; Pan, J. (2017): Probability of debonding and effective elastic properties of particle-reinforced composites. *Journal of Mechanics*, vol. 33, no. 6, pp. 789-796.

Dhaliwal, R.; Sherief, H. (1980): Generalized thermoelasticity for anisotropic media. *Quarterly of Applied Mathematics*, vol. 33, pp. 1-8.

Kant, T.; Swaminathan, K. (2000): Estimation of transverse/interlaminar stresses in laminated composites- a selective review and survey of current developments. *Journal of Composites*, vol. 49, pp. 65-75.

Lajczok, M. R. (1986): New approach in the delamination of interlaminar shear stresses from the results of MSC/NASTRAN. *Computers and Structures*, vol. 24, pp. 651-656.

Lekhnitskii, S. G. (1981): *Theory of Elasticity of an Anisotropic Body*. Mir Publishers, Moscow.

Lin, J.; Chen, W.; Chen, C. S. (2014): Numerical treatment of acoustic problems with boundary singularities by the singular boundary method. *Journal of Sound and Vibration*, vol. 333, no. 14, pp. 3177-3188.

Lin, J.; Chen, W.; Wang, F. Z. (2011): A new investigation into regularization techniques for the method of fundamental solutions. *Mathematics and Computers in Simulation*, vol. 81, no. 6, pp. 1144-1152.

Lin, J.; Zhang, C.; Sun, L. L.; Lu, J. (2018): Simulation of seismic wave scattering by embedded cavities in an elastic half-plane using the novel singular boundary method. *Advances in Applied Mathematics and Mechanics*, vol. 10, no. 3, pp. 322-342.

Lo, K. H.; Christensen, R. M.; Wu, E. M. (1978): Stress solution determination for higher order plate theory. *International Journal of Solids and Structures*, vol. 14, pp. 655-662.

Shiah, Y. C. (2016): Analysis of thermoelastic stress-concentration around oblate cavities in three-dimensional generally anisotropic bodies by the boundary element method. *International Journal of Solids and Structures*, vol. 81, pp. 350-360.

Shiah, Y. C.; Wang, S. H. (2016): New domain integral transformation in the boundary element analysis for 2D anisotropic thermoelasticity. *Journal of Engineering Mechanics*, vol. 142, no. 9, pp. 1-9.

Shiah, Y. C.; Ye, S. Y. (2016): New treatment of the self-weight and the inertial effects of rotation for the BEM formulation of 2D anisotropic solids. *Engineering Analysis with Boundary Elements*, vol. 73, pp. 170-180.

Shiah, Y. C.; Hematiyan, M. R. (2018): Interlaminar stresses analysis of three-dimensional composite laminates by the boundary element method. *Journal of Mechanics*, vol. 34, no. 6, pp. 829-837.

Shiah, Y. C.; Hsu, C. L.; Hwu, C. (2018): Analysis of 2D anisotropic thermoelasticity involving constant volume heat source by directly transformed boundary integral equation. *Engineering Analysis with Boundary Elements*, vol. 93, pp. 44-52.

Shiah, Y. C.; Hwu, C.; Yao, J. J. (2019): Boundary element analysis of the stress intensity factors of plane interface cracks between dissimilarly adjoined anisotropic materials. *Engineering Analysis with Boundary Elements*, vol. 106, pp. 68-74.

Shiah, Y. C.; Tuan, N. A.; Hematiyan, M. R. (2018): Direct transformation of the volume integral in the boundary integral equation for treating three-dimensional steady-state anisotropic thermoelasticity involving volume heat source. *International Journal of Solids and Structures*, vol. 143, pp. 287-297.

Tokovyy, Y. V.; Ma, C. C. (2017): Three-dimensional elastic analysis of transversely-isotropic composites. *Journal of Mechanics*, vol. 33, no. 6, pp. 821-830.

Tolson, S.; Zabaras, N. (1991): Finite element analysis of progressive failure in laminated composite plates. *Computers and Structures*, vol. 38, pp. 361-376.

Wen, P. H.; Alliabadi, M. H.; Rooke, D. P. (1998): A new method for transformation of domain integrals to boundary integrals in boundary element method. *Communications in Numerical Methods in Engineering*, vol. 14, pp. 1055-1065.